Difference imaging of adenovirus: bridging the resolution gap between X-ray crystallography and electron microscopy

Phoebe L.Stewart[1], Stephen D.Fuller[2] and Roger M.Burnett[1,3]

[1]The Wistar Institute, 3601 Spruce Street, Philadelphia, PA 19104, USA and [2]Biological Structures and Biocomputing Programme, European Molecular Biology Laboratory, Meyerhofstrasse 1, D6900 Heidelberg, Germany

[3]Corresponding author

Communicated by L.Philipson

While X-ray crystallography provides atomic resolution structures of proteins and small viruses, electron microscopy provides complementary structural information on the organization of larger assemblies at lower resolution. A novel combination of these two techniques has bridged this resolution gap and revealed the various structural components forming the capsid of human type 2 adenovirus. An image reconstruction of the intact virus, derived from cryo-electron micrographs, was deconvolved with an approximate contrast transfer function to mitigate microscope distortions. A model capsid was calculated from 240 copies of the crystallographic structure of the major capsid protein and filtered to the correct resolution. Subtraction of the calculated capsid from the corrected reconstruction gave a three-dimensional difference map revealing the minor proteins that stabilize the virion. Elongated density penetrating the hexon capsid at the facet edges was ascribed to polypeptide IIIa, a component required for virion assembly. Density on the inner surface of the capsid, connecting the ring of peripentonal hexons, was assigned as polypeptide VI, a component that binds DNA. Identification of the regions of hexon that contact the penton base suggests a structural mechanism for previously proposed events during cell entry.

Key words: adenovirus/cryo-electron microscopy/difference imaging/image reconstruction/X-ray crystallography

Introduction

The structure determination of large macromolecular assemblies poses a challenge for modern biology. Many basic biochemical processes, including DNA transcription and translation, the immune response, cellular transport and virus assembly, involve the concerted action of large numbers of components. Understanding the three-dimensional organization of these components, as well as their detailed atomic structures, is central to the interpretation of their function. X-ray crystallography and NMR spectroscopy have provided atomic structures of proteins, stretches of nucleic acid, DNA−protein complexes and viruses. Image reconstruction combined with electron microscopy (EM) has yielded three-dimensional structures of large viruses and macromolecular assemblies at lower resolution.

Unfortunately, as the boundaries between the various components in the reconstruction of a complex assembly are usually unclear, it is often difficult to interpret the density and assign it to specific structural components. This limitation can be alleviated with three-dimensional difference imaging. We demonstrate for adenovirus the power of combining EM of a complex with X-ray crystallography of a single component.

Adenovirus, first isolated in 1953 in human adenoidal tissue (Rowe et al., 1953), is a common cause of respiratory infections. Various types of adenovirus cause conjunctivitis and enteric dysentery, a leading killer of Third World infants. Human type 2 adenovirus is a large macromolecular assembly, 1400 Å in diameter, composed of at least 11 different structural proteins (polypeptides II−IX, IIIa, μ, terminal) and a linear double-stranded DNA genome. The structure of the isolated major capsid protein, hexon, has been solved to 2.9 Å resolution by X-ray crystallography (Roberts et al., 1986; F.K.Athappilly, R.Murali, Z.Cai and R.M.Burnett, in preparation) and refined by simulated annealing (R.Murali and R.M.Burnett, in preparation). Recently, the structure of the intact virus was solved to 35 Å resolution by image reconstruction from cryo-electron micrographs (Stewart et al., 1991). The distinctive shape of the hexon molecule, known from crystallography, was clearly visible for all 240 copies of hexon in the reconstruction.

The similarity of hexon's features when imaged by crystallography and EM is striking. This property was exploited in our first combined structural approach using scanning transmission electron microscope (STEM) images of a capsid dissociation fragment known as the group-of-nine hexons (Furcinitti et al., 1989). A two-dimensional difference image was calculated by subtracting an array of nine projected X-ray hexons from the STEM image, revealing density from a minor protein component extending along the hexon−hexon interfaces. Biochemical analysis showed this component to be polypeptide IX (van Oostrum and Burnett, 1985), a minor capsid protein involved in stabilizing the capsid (Colby and Shenk, 1981).

The success of two-dimensional difference imaging in revealing density that comprised just 6% of the total group-of-nine mass suggested that an extension of the technique to three dimensions would be profitable. Here we present a three-dimensional difference map, generated by subtracting 240 copies of the crystallographic hexon from the image reconstruction of adenovirus. The difference map has allowed density assignments for six different proteins in the adenovirus capsid, each at strategic positions; identified the atomic binding sites on hexon for the other structural proteins; and allowed the body of biochemical data on adenovirus assembly and uncoating to be interpreted in a new light.

Results

Three-dimensional difference imaging

It was quickly apparent that although the electron density maps obtained by the two structural techniques, X-ray crystallography and EM, were very similar, they displayed different detailed characteristics. X-ray crystallographic data are typically collected in the range of $1-10$ Å, while EM covers the range of $25-500$ Å for biological specimens. A necessary first step, before subtraction of the crystallographic component from the EM reconstruction, was to ensure that the two density maps matched as closely as possible. It was necessary to take into account differences in resolution, as well as distortions caused by the contrast transfer function (CTF) of the electron microscope, and various approaches were tried (as described in Materials and methods). The appearance of polypeptide IX, the small capsid component observed in two-dimensional difference images of a capsid fragment (Furcinitti *et al.*, 1989), provided a control for evaluating the correctness of the three-dimensional difference maps. Similarly, the features of the crystallographic hexon served as a control during the original image reconstruction (Stewart *et al.*, 1991).

In the earlier reconstruction of adenovirus, we combined data from low-, middle- and high-resolution images to compensate for the effects of the CTF. The resultant density was less noisy and qualitatively better than that obtained using the high-resolution data alone. In the current quantitative study, the match to the crystallographic hexon density was not good enough to provide an interpretable difference map. We found that the best approach was to recalculate the density using only the highest resolution cryo-electron micrographs so that an analytical deconvolution function could be applied (Figure 1A). The best parameters for the CTF equation were found by qualitatively observing the effect of different parameters on the crystallographic hexon density. For this purpose, a density map of the crystallographic hexon (Figure 2) was generated by summing the atomic numbers of the atoms in a hexon trimer within voxels the same size as those in the reconstruction (7.3 Å³). An approximate CTF was used to deconvolve the image reconstruction and generate undistorted density for the intact virus. The deconvolution included a 25 Å low-pass filter to remove noise. A portion of the deconvolved image reconstruction, roughly equal to two facets of the icosahedral capsid, is shown in Figure 1B.

The crystallographic hexon density map, also filtered to the 25 Å resolution (Figure 2C), was used as a probe to find the orientations of the four hexons in the asymmetric unit (1/60) of the viral capsid. The hexon bases merge to form the protective protein shell and so only the protruding tower region was used as a search model. The hexon positions were
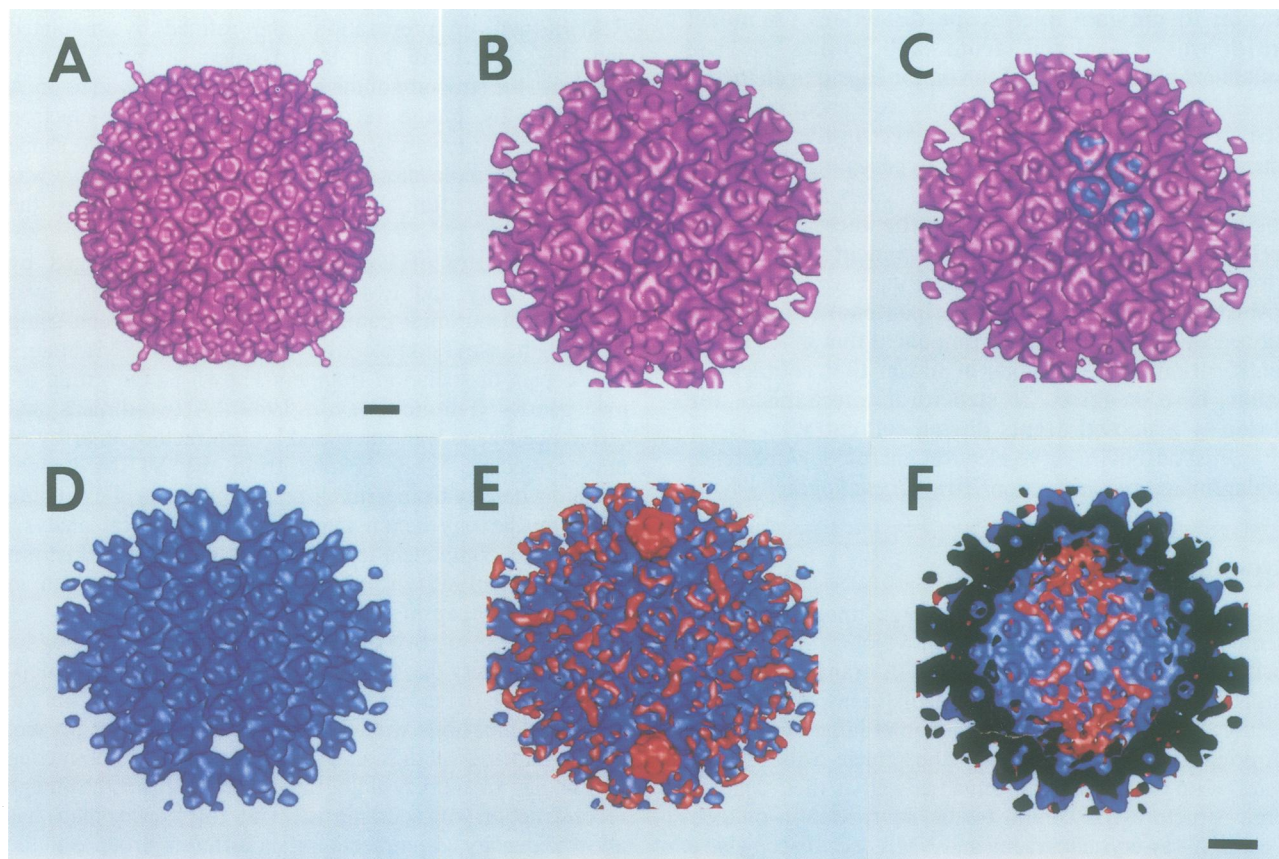

Fig. 1. Views of the adenovirus reconstruction, calculated hexon capsid and difference map. (A) A surface view of the complete image reconstruction of adenovirus calculated from high-resolution (close to focus) cryo-electron micrographs. The viewing direction is along an icosahedral 2-fold axis. (B) An enlarged view of a portion of the reconstruction after deconvolution by an approximate CTF of the electron microscope. (C) Tower regions of four crystallographic hexons (blue) positioned into four independent locations in the icosahedral asymmetric unit. (D) A portion of the calculated capsid of hexons based on the crystallographic coordinates. The gaps in the density at the vertices are filled by pentons in the intact virus particle. (E) An external view of the difference map (red) superimposed on the calculated hexon capsid density (blue). (F) An internal view of the difference map at a slightly higher contour level than in (E) to reveal separate components. The scale bars are 100 Å.
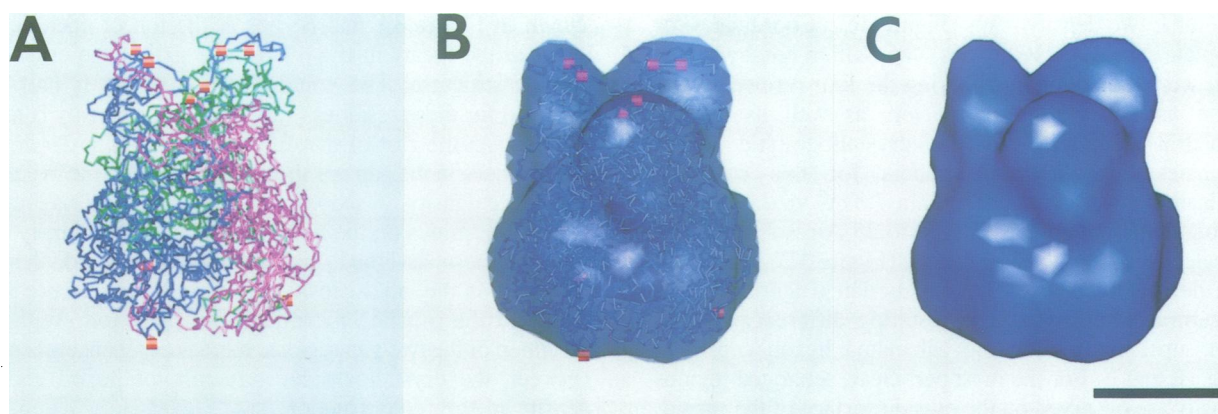
Fig. 2. Views of the major coat protein, hexon. (A) The C_α backbone of the hexon trimer with each monomer in a different color. The missing residues in the crystallographic model at the N-terminus (residues 1−43) and in an internal gap (273−291) are marked with red squares at residues 44, 272 and 292. (B) The C_α backbone of the hexon trimer within a transparent envelope of hexon density derived from the crystallographic coordinates and filtered to 25 Å resolution. The missing stretches are marked with red squares. (C) A surface representation of the crystallographic hexon density filtered to 25 Å resolution. The scale bar is 50 Å.
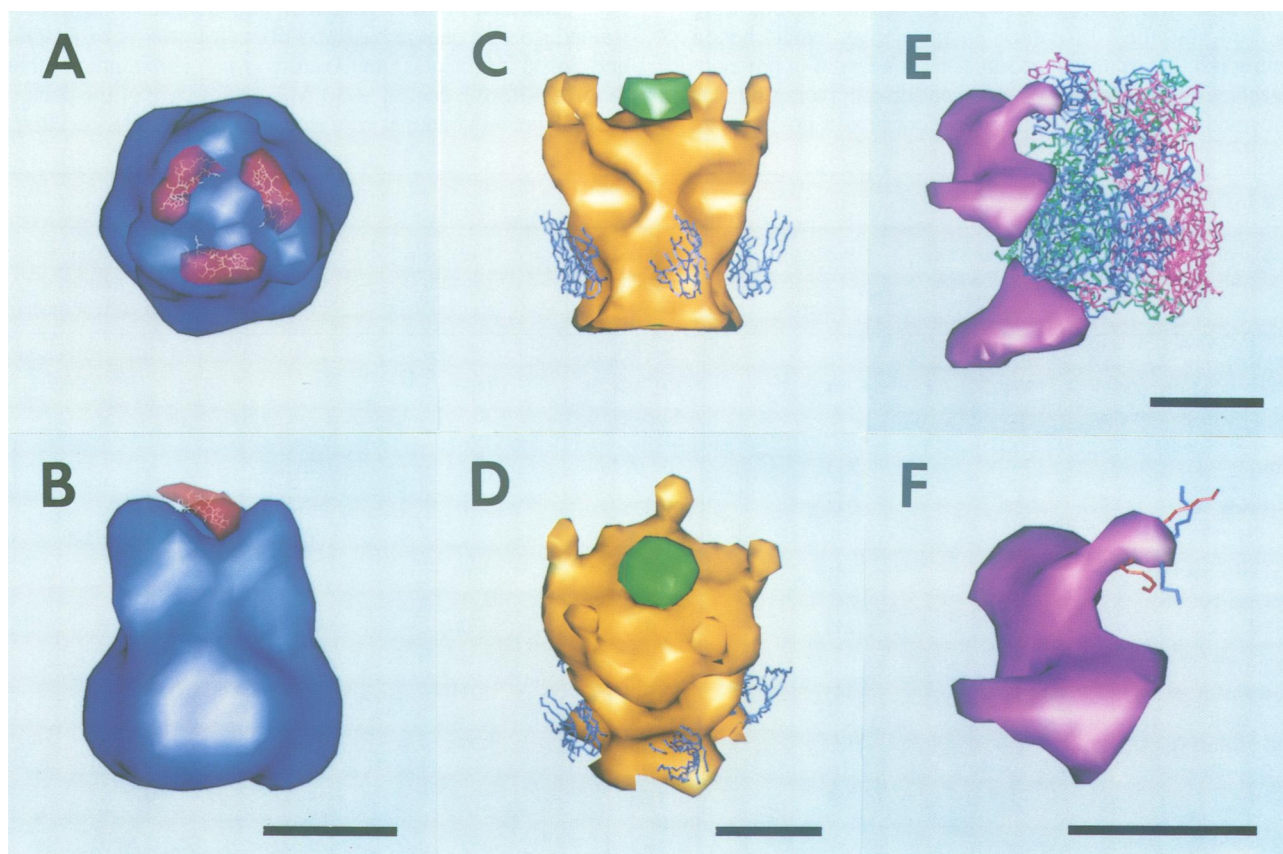

Fig. 3. Views of difference density corresponding to hexon, penton complex and polypeptide IIIa. (A) A top view of the crystallographic hexon density in blue with the averaged difference density above the towers in transparent red. Three copies of the 19 residue internal gap in the crystallographic hexon structure in white are shown modeled into the difference density. The averaged difference density is shown with a contour level slightly lower than that chosen for the volume measurements so that it has the full predicted volume. (B) A side view of the crystallographic hexon density with one-third of the averaged difference density and one copy of the modeled 19 residue gap. (C) A side view of the penton base (yellow) and fiber (green) with the P1 β-barrels of the five surrounding peripentonal hexons shown as C_α backbones (blue). (D) A tilted view of the penton base, fiber and hexon β-barrels. Note that the β-barrels fit into grooves near the bottom of the penton base. (E) A side view of the density assigned to polypeptide IIIa (purple) next to a C_α backbone of the crystallographic hexon trimer. The density spans the capsid and has both an internal and an external domain. The polypeptide IIIa density is shown with a slightly lower contour level than Figure 3C and D so that the protruding arm density is connected. Note the tapering of the density in the middle of the capsid. (F) An enlarged view of the external density assigned to polypeptide IIIa with the hexon residues near the region of contact with the protruding arm. Hexon residues (255−272) are shown in red and residues (292−305) from the same monomer are shown in blue. The scale bars are 50 Å.

refined by maximizing the cross-correlation coefficient between the two density maps (Figure 1C). Coordinates for a complete capsid of 240 hexons, >5 million non-hydrogen atoms, were generated by applying the four refined sets of rotation and translation parameters as well as 60-fold icosahedral symmetry to the crystallographic hexon coordinates. The atomic numbers for this complete coordinate set were summed within 7.3 Å³ voxels and the resulting density map was filtered to 25 Å resolution. The final calculated hexon capsid density (Figure 1D) was scaled to the deconvolved image reconstruction (Figure 1B) and then subtracted from it. The resulting difference map is shown superimposed on the calculated hexon capsid in Figure 1E and F. For the most part clear, separated regions of density are observed on the outside surface of the capsid. The inside surface of the capsid, or DNA view, is complicated by the presence of weak, less well-ordered, density regions that connect the capsid to the disordered core.

Hexon (polypeptide II)

The crystallographic hexon trimer and the 25 Å resolution density map derived from the atomic coordinates are shown in Figure 2. Small, irregularly shaped density regions were observed in the difference map above each hexon (Figure 1E). To improve the signal-to-noise ratio of any non-artifactual density in this location, additional averaging was performed among the four independent hexon positions as described in Materials and methods. The resulting density, shown in Figure 3A and B, lies at the top of each hexon tower at the location of a 19 residue gap in the crystallographic structure. The volume of this region is half that expected for these residues (Table I), but its density is more diffuse than the rest of the difference map. The 19 amino acid residues in the gap are shown modeled into the averaged difference density. A second gap, of 43 residues, is located at the N-terminus on the base of the hexon. It is likely that some of the unassigned, and partially disordered, density observed on the inner capsid surface in the difference map is due to the mobile N-terminal arm of hexon. With the exception of the two gap regions, there is excellent agreement between the crystallographic structure of hexon and its density in the reconstruction.

Penton base (polypeptide III)

The penton complex, at the 12 vertices of the capsid, is cut from the difference map in Figure 4A and B. The penton is composed of a pentameric base of polypeptide III and a trimer of polypeptide IV that forms the protruding fiber (van Oostrum and Burnett, 1985). The two components have not been separated by difference imaging. Images of negatively stained isolated penton base and fiber (Ruigrok et al., 1990) and capsid fragments (van Oostrum et al., 1987) indicate that the fiber fills the central ~30 Å diameter core of the penton base. Thus a cylinder with a diameter of 4 pixels, or 29 Å,

Table I. Capsid components

Polypeptide	Measured vol. of monomer (voxels)	Predicted vol. of monomer (voxels)[a]	Molecular mass of monomer (Da)[b]	Number of residues in monomer[b]	Biochemical copy number of monomer[b]	Copy number of monomer in current model
II (hexon)						
905 residues in model	394	394	102 050	905		
43 residue N-terminus	−[c]	19	4898	43		
19 residue gap	4	8	2129	19		
Total	−	421	109 077	967	720 ± 7	720
III (penton base)	228	244	63 296	571	56 ± 1	60
IIIa						
External portion	157	161	41 689	376[d]		
Internal portion	81	84	21 846	194[d]		
Total	238	245	63 535[e]	570[e]	68 ± 2[e]	60
IV (fiber)						
N-terminus + 2/8 of shaft	54	54	13 912	133[d]		
6/8 of shaft + C-terminus	−	185	48 048	449[d]		
Total	−	239	61 960	582	35 ± 1	36
VI						
Ordered portion	44	38	9773	91[d]		
Disordered portion	−	48	12 345	115[d]		
Total	−	86	22 118[e]	206[e]	342 ± 4[e]	360
VIII	−	59	15 390[e]	140[e]	127 ± 3[e]	−
IX	29	55	14 339	139	247 ± 2	240

[a]The observed volume to molecular mass ratio of the 905 residues in the hexon crystallographic model was used to predict the volumes of the other capsid components based on their molecular masses.
[b]The molecular masses, residue numbers and biochemically determined copy numbers for the monomers are from van Oostrum and Burnett (1985), and updated with adenovirus proteinase cleavage sites from Anderson (1990) as noted.
[c]The dashes indicate density not assigned in the three-dimensional difference map.
[d]Estimated division.
[e]Includes the effect of updated adenovirus proteinase cleavage sites (Anderson, 1990).

was used to crop the fiber from the center of the penton base. The boundary between the penton base and internal ring of polypeptide VI was estimated at the point of the narrowest diameter for optimal agreement with the spade-like shape of the penton base in negative-stain images.

The cropped penton base has a height of 124 Å, including the five small protrusions at the top, as well as maximum and minimum diameters of 112 and 50 Å, in reasonable agreement with Ruigrok *et al.* (1990). The five small protruding regions on the top of the penton base, which have not been observed previously, are ~22 Å in diameter. The volume of the cropped penton base is 93% of that predicted from its molecular mass by extrapolation from the measured volume and molecular mass of hexon (Table I). However, the volume measured for the penton base is critically dependent on where the boundaries are set between it and its adjoining components. When the lower boundary of the penton base is varied by ±1 pixel, the volume fluctuates by 8%. This is the largest source of error in the measurement; varying the CTF parameters (see Materials and methods) yields a much smaller volume fluctuation of 3%.

The interface between the penton base and the peripentonal

hexon can be examined in atomic detail on the hexon side of the interaction. There are two β-barrels in the base of the hexon monomer labeled P1 and P2 (Roberts *et al.*, 1986). In the viral capsid, the hexons are rotated so that the P1 β-barrels fit into grooves on the side of the penton base. The C_α backbone of the P1 β-barrel is shown next to the penton base in Figure 3C and D.

Fiber (polypeptide IV)

The density cropped from the cylindrical core of the penton base is shown in Figure 4B. Its volume is just 23% of that predicted for the entire trimeric fiber; however, the fiber is bent and thus improperly averaged in the reconstruction. After deconvolution, the fiber is even shorter than in the original reconstruction with just 20 Å of the shaft protruding outside the penton base. Ruigrok *et al.* (1990) showed that the complete fiber protrudes ~330 Å from the penton base. The cropped fiber shows two internal density 'beads' and a third roughly spherical region protruding from the top of the penton base. The spacings between the centers of density in the cropped fiber are 56 Å between the two innermost spheres, and 45 Å between the two outermost spheres. A
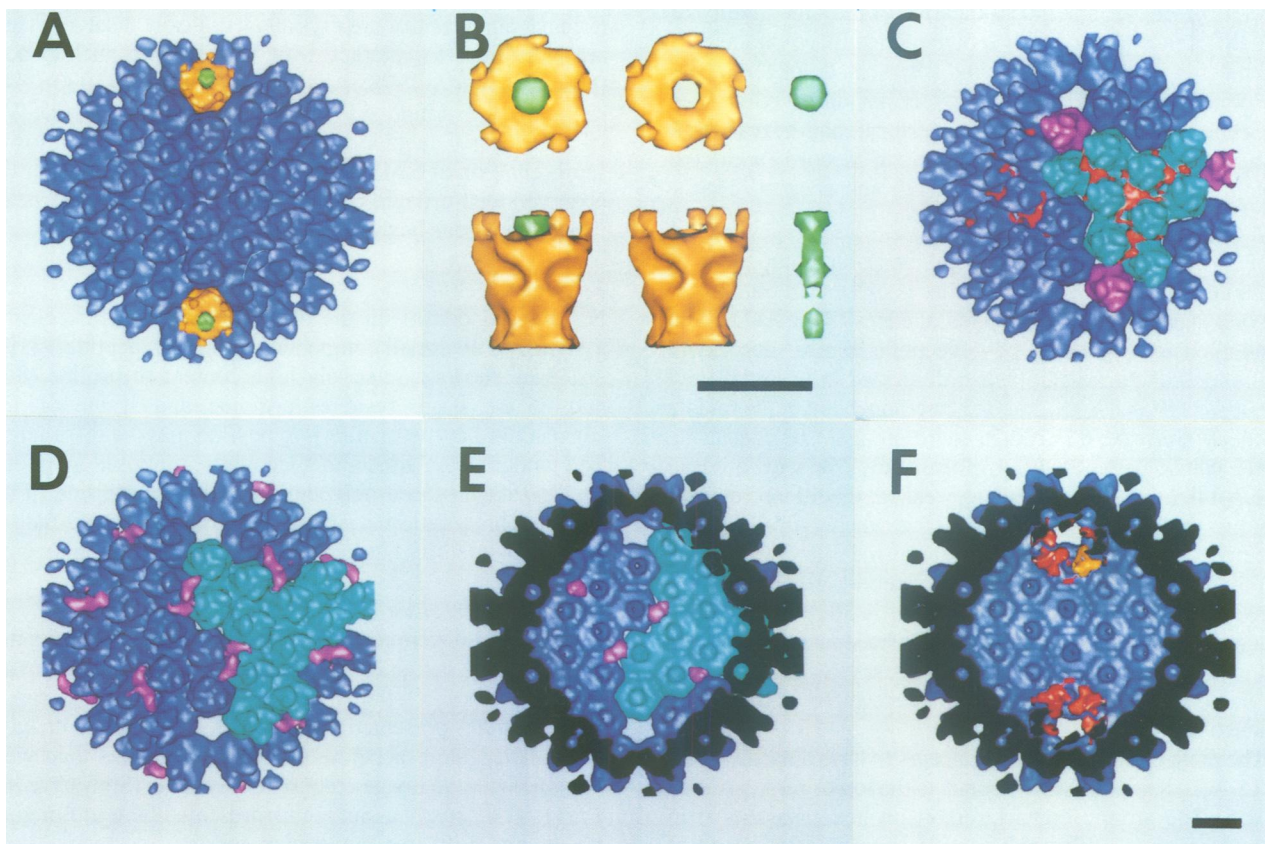

Fig. 4. Views showing penton base, fiber, polypeptides IX, IIIa and VI. **(A)** The penton base (yellow) and fiber (green) cropped from the difference map superimposed on the hexon capsid (blue). **(B)** Top and side views of the penton base and fiber. Note the five small protrusions on the top of the penton base. The fiber density is shown with a slightly higher contour level than that used for the volume measurement to accentuate the beading pattern. **(C)** The density assigned to polypeptide IX (red) superimposed on the hexon capsid with nine hexons in the center of one facet in light blue and three peripentonal hexons in purple. The density is rotated so that the view is along an icosahedral 3-fold axis. Note that polypeptide IX stabilizes the central group-of-nine hexons. **(D)** The density assigned to the external portion of polypeptide IIIa (purple) superimposed on the hexon capsid with one facet of 12 hexons in light blue. Note that polypeptide IIIa stabilizes the junction between two facets. **(E)** The density assigned to the internal portion of polypeptide IIIa as viewed from the inside of the capsid. **(F)** The density assigned to polypeptide VI, with one 3-fold region in yellow and the rest in red, superimposed on the hexon capsid. The view is from the inside of the capsid. For consistency with the other figures, only a portion (~4/5) of the ring of density assigned to polypeptide VI is shown around each of the two vertices in this partial capsid. The cleavage plane where the capsid is cut appears black. The polypeptide VI density is shown with a slightly higher contour level than the other components in the difference map so that only the well-ordered density is observed. The scale bars are 100 Å.

beading pattern was also observed in negatively stained isolated fibers with 7−9 beads along the shaft spaced by ~35 Å and not counting the larger C-terminal knob (Ruigrok et al., 1990).

Analysis of the primary sequence of the adenovirus type 2 fiber by Green et al. (1983) suggested an N-terminal portion of 44 residues, a shaft of 357 residues with a highly repetitive sequence of 22 segments and a C-terminal head of 181 residues forming the knob at the distal end of the fiber. If the shaft corresponds to eight density beads, each composed of two or three sequence repeats and spaced by an average distance of 40 Å to yield the correct overall length, then each bead would be ~8% of the total molecular mass. The cropped fiber density has roughly the correct volume if the innermost bead is the N-terminal portion and the two outermost density beads are 2/8 of the shaft (Table I).

Polypeptide IX
The polypeptide IX density cut from the difference map is shown in Figure 4C. Four trimeric regions are found on the outer capsid surface at locations between the nine hexons in the center of one facet. Only the central trimer has been 3-fold symmetrized by the reconstruction process as it lies directly on an icosahedral symmetry axis. The 3-fold nature of the other trimers is thus indicative of the high quality of the difference map. One polypeptide IX monomer is estimated to be 64 Å long and 18 Å in diameter at the midpoint. Polypeptide IX density is not observed at sites adjacent to each of the three peripentonal hexons that complete a facet of 12 hexons, in accord with the stoichiometric analysis (van Oostrum and Burnett, 1985).

Polypeptide IIIa
The difference map reveals a large elongated component on the outer surface of the capsid that is present in 60 copies, two along each of the 30 icosahedral edges (Figure 4D). The assignment of this density to polypeptide IIIa is in agreement with the updated stoichiometry, described in Materials and methods. The density appears to taper to a point in the middle of the hexon capsid and then to begin again on the inside of the capsid (Figure 3E). Unfortunately, the well-ordered internal density is connected to weaker, disordered density making the boundary uncertain; but when only the well-ordered density is included, the total measured volume is within 3% of that predicted for polypeptide IIIa. The outer density region has an irregular shape, ~30 Å in diameter, that reaches 50 Å above the capsid surface and has contacts with four different hexons. Its inner density region is ~37 Å in diameter and lies at the point where three hexons meet (Figure 4E).

The polypeptide IIIa density appears to have a narrow arm, ~15 Å in diameter, which contacts the tower region of one hexon. The atomic contact region on hexon is shown in Figure 3E and F. The polypeptide IIIa arm sits on top of a small kink at the base of a β-strand in the hexon tower region. The kink is composed of residues 255−261, which are highly conserved among the four human adenovirus hexons that have been sequenced (Toogood et al., 1989). The β-strand residues above the kink, 262−267, are highly variable among the four hexon sequences and appear to pass through the polypeptide IIIa density and could represent a type-specific binding site. A second, largely conserved β-strand (residues 292−305) also passes through the tip of the polypeptide IIIa arm density.

Polypeptide VI
Much of the difference density on the inner capsid surface is irregular in shape and difficult to interpret. An exception is a region showing a clear trimeric shape that connects the bases of adjacent peripentonal hexons (Figure 4F). Three density lobes, ~29 Å in diameter, are spaced by 46 Å from each other. This local 3-fold symmetry was not imposed by the icosahedral averaging applied during image reconstruction and was not apparent until after deconvolution. Volume measurement of the trimeric region indicates that the region has roughly the correct volume for a trimer of polypeptide VI, while the stoichiometry indicates it should be a hexamer (Table I). This apparent contradiction is resolved if only half of the mature polypeptide is ordered and each density lobe in the trimeric region corresponds to a dimer of polypeptide VI.

Support for this hypothesis is found in the sequence. A stretch of 115 residues in the middle of the mature polypeptide is moderately basic (13% arginine and lysine) and highly proline rich (21%), making it similar to the 113 residue N-terminal domain of the Sindbis virus core protein. This domain, which is 19% proline and 26% arginine or lysine, is disordered in the crystallographic structure (Choi et al., 1991). Many viral capsid proteins have basic N-terminal domains that are crystallographically disordered and are presumed to interact with the internal nucleic acid (Harrison et al., 1978; Abad-Zapatero et al., 1980). The remaining 91 amino acids in the mature polypeptide VI, which do not include any prolines and have a lower representation of basic residues (9%), could account for the observed well-ordered density that forms a ring underneath the peripentonal hexons.

Polypeptide VIII
No ordered density in the difference map can be clearly assigned to this small component. As in polypeptide VI, the sequence shows a relatively high content of proline (8%) and of the basic residues arginine and lysine (11%), suggesting that the mature polypeptide may be disordered. The topographical model of adenovirus, proposed by Everitt et al. (1975), placed polypeptide VIII on the inside of the capsid. This location is supported by the difference map as all external density has been assigned to other components.

Overall architecture
All assigned difference density is shown in Figure 5A and B in both internal and external capsid views. A schematic representation of the locations of the minor capsid components is presented in Figure 5C. Difference imaging has allowed more accurate density assignments than were possible with the image reconstruction alone (Stewart et al., 1991). The density assignments presented here are in good agreement with the molecular masses, corrected copy numbers and biochemical information on the structural components.

Discussion

Comparison of EM and crystallographic hexon structures
The ability to subtract multiple copies of the crystallographic hexon structure from the EM density and obtain an interpretable three-dimensional difference map is strong
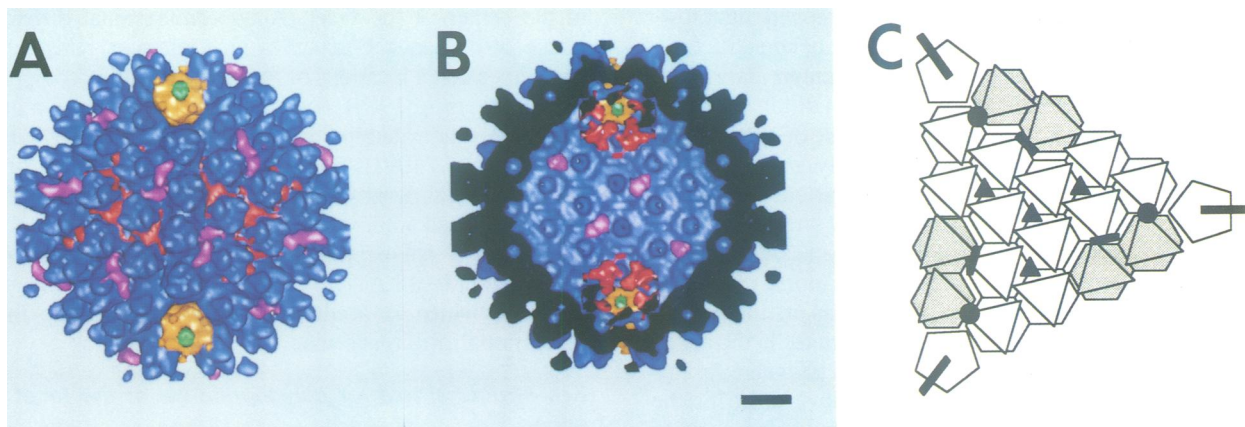
Fig. 5. Views showing the overall organization of the adenovirus virion. **(A)** An external view of the capsid components observed in the difference map. All components are shown at the contour level chosen for the volume measurements and colored as in Figure 4. **(B)** An internal view corresponding to (A). The density assigned to polypeptide VI (red) is shown at a higher contour level than that chosen for the volume measurement so that only the well-ordered density is observed. The scale bar is 100 Å. **(C)** A diagram of the adenovirus facet showing the locations of the capsid components in the current model. The 12 hexons in the complete facet are shown as white triangles superimposed on hexagons. The edge hexons from adjacent facets are shown as shaded symbols. The penton bases are depicted as pentagons with long bars representing the protruding fibers. The polypeptide IX trimers on the outer capsid surface are represented as triangles. The polypeptide IIIa monomers passing through the capsid are represented as short bars. The polypeptide VI hexamers on the inside of the capsid are represented as circles.

support for the quality of the EM density. A fundamental assumption for the success of this combined structural approach was the similarity of the hexon structure in the crystal at pH 5.0 and in the reconstruction of the intact virus at pH 8.1. We were forced to use two different pH values as the intact virus is unstable below pH 8.1 and the hexon crystals crack above pH 5.5. A structural change in the intermediate pH range is suggested by the observation that the bacterial endoproteolytic enzyme dispase cleaves type 2 hexons at pH 5.0 but has a negligible effect at pH 7.5 (Varga et al., 1990). However any pH-dependent structural change in hexon must be beyond the resolution limit of the difference map. A crystallographic study of the effect of pH on the hexon structure is underway (R.Murali, J.J.Rux and R.M.Burnett, unpublished results).

One obvious difference between the EM and crystallographic hexons is that the crystallographic model lacks 19 residues at the top of the tower and 43 residues at the N-terminus, while the EM density corresponds to the entire polypeptide. Density was observed in the difference map for the 19 residues at the top of the hexon tower, which are too mobile to be observed by crystallography. These residues, 273–291, are interesting as they contain a neutralizing type-specific antigenic determinant (Toogood et al., 1992). If these residues, which are exposed on the outer surface of the virus, are in somewhat different orientations in each hexon this would explain the non-uniform appearance of the difference density at the hexon tops and the connected appearance of the hexon towers in the original reconstruction (Stewart et al., 1991). By averaging the independent regions, a spatially averaged density map representing the predominant conformation is obtained. Using model building and molecular dynamics, a plausible atomic structure for the 19 residues was fit into the observed difference density to model the epitope. The observation of this density highlights the potential power of the combined structural technique, as the sum of the hexon gap density in the capsid is <1% of the total mass of the particle.

Structural components of the adenovirus capsid

Three-dimensional difference imaging of adenovirus has revealed an architecture that is notable for the presence of a minor stabilizing component at each specialized location in the hexon capsid. In addition to the penton complex, which fills the large gaps left at the vertices: polypeptide IX stabilizes hexon–hexon contacts within the center of a facet; polypeptide IIIa joins hexons of adjacent facets and spans the hexon capsid; and polypeptide VI anchors the ring of peripentonal hexons on the inside surface of the capsid as well as connecting the highly ordered capsid to the core. Polypeptide VIII is the only capsid protein that cannot be assigned in the difference map. Its small size and relatively low copy number contribute to the difficulty of the assignment, but it is likely that this basic component is on the inside of the capsid where loosely ordered density is found and accurate volume measurements are not possible. These assignments, together with the updated molecular masses and copy numbers, are presented in Table I. As the crystallographic hexon coordinates have been positioned within the EM density, the interfaces that hexon makes with other components may now be examined at an atomic level on the hexon side. The hexon–hexon interfaces themselves are completely defined and are currently being analyzed.

Dissociation of the penton complex during cell entry

The difference map gave the first clear view of the penton complex located on the capsid vertices. The penton complex is important structurally, as it completes the icosahedral capsid formed predominantly by hexons, and functionally, as it has been implicated in disruption of the endosomal membrane after receptor-mediated endocytosis (Seth et al., 1984; Varga at al., 1991). Penetration of the membrane and release of the virus into the cytoplasm is thought to involve a pH-dependent conformational change of the capsid within the acidic endosome (Wohlfart, 1988). Wohlfart has proposed that neutralizing anti-penton base antibodies act by covering the penton base and preventing its interaction with the endocytic membrane. He has also suggested that

neutralizing anti-hexon antibodies act by preventing a low-pH-induced conformational change in the hexon structure, so inhibiting the proper exposure of penton base. The difference imaging results allow evaluation of this proposed cell entry pathway from a structural point of view.

The adenovirus type 2 hexon has a highly unusual stretch of 16 sequential glutamates and aspartates, residues 146−161, which are directly above the D strand of the P1 β-barrel (Roberts et al., 1986). The three acidic stretches in the trimer are just 17 Å apart at the point of closest approach. We assume that at pH 5.0, as in the crystal structure, most of the glutamates and aspartates in the acidic stretches are protonated since the estimated pK value for this region is 5.5 (Burnett et al., 1985). Above pH 5.5, the glutamates and aspartates must become charged and create an electrostatic repulsion between the three acidic stretches. We postulate that this would cause an outward tilt of the top of the P1 β-barrel. The crystallographic structure of hexon shows that the six β-barrels in the trimer are more tightly intertwined at their bases than at their tops (Roberts et al., 1986). The difference imaging results show that the side of the P1 β-barrel is in contact with the penton base, thus a subtle pH-induced structural shift, which could be magnified in the virus by the concerted action of all 240 hexons, could result in the release of the penton base at low pH. A similar pH-dependent concerted structural change has been observed for tomato bushy stunt virus (Robinson and Harrison, 1982) and other spherical plant viruses (Bancroft, 1970). Interestingly, the acidic stretch is absent in the hexons of types 40 and 41 adenoviruses (subgroup F) (Toogood et al., 1989), despite strong overall homology between subgroups. This suggests that the cell entry pathway for subgroup F, which causes enteric dysentry, may be different to that for subgroup C (types 2 and 5), which causes respiratory infections. A striking difference between these two subgroups is the inability of subgroup F adenoviruses to grow in conventional cell lines (de Jong et al., 1983).

Comparison of the EM density with a fiber model

The fiber density cut from the central core of the penton complex in the difference map can be used to evaluate a recently published model structure for the fiber shaft (Stouten et al., 1992). The model predicts that the three identical polypeptide chains form a left-handed triple-helical structure with an outer diameter of 28 Å. Short β-strands of three residues are interspersed with extended loops of 3−11 residues that continue the overall helical path. The model building assumed that the central core of the fiber was not hollow. The difference density confirms this assumption, as well as the diameter of the fiber model. Only one modification of the model is required for complete agreement with the density. The density beads observed in the original image reconstruction (Stewart et al., 1991), in the difference density reported here, and in fibers rotary shadowed with platinum (Ruigrok et al., 1990), can be explained if some of the extended loops do not follow the helical fold. Perhaps packing strain accumulates for the hydrophobic side chains that point towards the interior of the fiber and this can only be relieved by periodically breaking the tight helical packing.

Three-dimensional location of polypeptide IX, the capsid cement

The difference map revealed density from polypeptide IX, the minor component stabilizing the group-of-nine hexons

in the center of the facet. A two-dimensional difference image of the isolated group-of-nine complex revealed the two-dimensional locations of four trimers of this component (Furcinitti et al., 1989), and the image reconstruction of the intact virus indicated that it was on the outer capsid surface (Stewart et al., 1991). The measured volume of the discrete polypeptide IX density in the difference map is only 53% of the predicted volume. The most likely explanation is that the width of polypeptide IX, as observed in the higher resolution (15−18 Å) two-dimensional difference image, is <25 Å, which is at the resolution limit of the three-dimensional difference map.

Key structural role for polypeptide IIIa at the facet edges

The location of polypeptide IIIa, one of the three largest protein components in adenovirus, has been controversial. Early biochemical studies suggested that it was released along with the peripentonal hexons, those next to the penton (Everitt et al., 1973). However, interpretation of the data was difficult as the polypeptide IIIa band was incompletely resolved from the polypeptide IV band on SDS gels. A subsequent estimate of 60 copies of polypeptide IIIa per virion (Boudin et al., 1980) led to a model with monomers of polypeptide IIIa between the peripentonal hexons and the penton base. A later stoichiometric analysis (van Oostrum and Burnett, 1985) using high-resolution gradient gels, showed that polypeptide IIIa is not released with the penton and peripentonal hexons, placing doubt on the assumption that polypeptide IIIa is located in the vertex region. The original image reconstruction of the intact virus did not reveal the position of polypeptide IIIa because of the difficulty in separating the different protein components (Stewart et al., 1991).

The difference map has allowed assignment of polypeptide IIIa to an unexpected, but structurally reasonable, location at the facet edge. Elongated density regions were observed on the outside of the hexon capsid tapering off above well-ordered density on the inside of the capsid. The possibility that polypeptide IIIa spans the hexon capsid was first suggested by Everitt et al. (1975), and electron micrographs of negatively-stained recombinant polypeptide IIIa in 1 M urea reveal it to be long enough (200 Å) to span the capsid (Cuillel et al., 1990). The diameter of the recombinant polypeptide, 28 Å, is also similar to that observed in the difference map. The fact that the C-terminal end of the IIIa precursor is cleaved by the adenovirus proteinase, which is most likely contained in the interior of the viral particle, suggests that this end corresponds to the internal density. The location of polypeptide IIIa is biologically significant as temperature-sensitive mutant virions defective for this polypeptide are trapped as empty capsids during viral assembly (Boudin et al., 1980).

Polypeptide VI connects the capsid to the nucleo-protein core

The assignment of polypeptide VI to the inside of the capsid is consistent with the known non-specific binding of this component to DNA (Russell and Precious, 1982), as well as with the cleavage of both termini by the adenovirus proteinase. Clear trimeric density regions are observed securing the ring of peripentonal hexons. A trimer of dimers, where each lobe corresponds to a dimer of polypeptide VI, is proposed to match the updated copy number (Table I).

Early biochemical evidence suggested that this component forms dimers (Everitt and Philipson, 1974), and a recent analysis of disulfide bond formation and protease cleavage is also consistent with a dimeric association (Webster *et al.*, 1993). The volume estimate, which is too low for six monomers, may be explained if a large portion of polypeptide VI is disordered through interactions with the internal DNA, which is not icosahedrally ordered.

This transition from an icosahedrally ordered capsid to a disordered nucleus may offer an explanation for the 12 large spheres observed in the core by ion etching (Newcomb *et al.*, 1984) and by EM of negatively stained preparations of sarcosyl cores (Brown *et al.*, 1975). If the ring of polypeptide VI, shown to be 160 Å in diameter, interacts with the internal viral DNA, it might tend to loosely order the DNA in a slightly larger circular region and cause differential staining effects in the core.

Complementarity of EM and crystallography

Combining the crystallographic hexon structure with the image reconstruction of the intact adenovirus particle has enabled a detailed analysis of the EM density. The crystallographic structure of the major capsid protein served as a control during the original image reconstruction (Stewart *et al.*, 1991) and enabled two-dimensional difference imaging of a capsid fragment (Furcinitti *et al.*, 1989), as well as three-dimensional difference imaging of the entire adenovirus capsid. Difference imaging has revealed the positions and low-resolution structures of all of the ordered capsid components. As the residues of hexon with which they interact have also been identified, structure-based drug design of peptides is now possible.

The major obstacle in generating an accurate and interpretable three-dimensional difference map was matching the density from the two techniques. We are confident that our approach has successfully bridged the resolution gap that previously existed between structural information from EM (25−100 Å) and X-ray crystallography (1−10 Å). Achievement of its full potential will rely on the development of better methods for correcting and combining electron micrographs. Even as imaging and computer processing techniques are improved, atomic resolution reconstructions may be unattainable due to thermal motion in the sample. Image reconstruction, however, has the potential to determine low-resolution structures of even unsymmetrical macromolecular complexes well beyond the current size limitations of X-ray crystallography and solution-state NMR. Thus, combining EM reconstructions of macromolecular complexes with atomic structures of their individual components will be essential for unraveling the chemical basis of biological function in large assemblies such as viruses, and even cellular organelles. The first major success of this combined approach is the clear identification of a set of structural proteins that act as cement in adenovirus. These may well be the first examples of a more general phenomenon.

Materials and methods

Deconvolution with the CTF

The effect of the CTF of the electron microscope is to accentuate a specific resolution range depending on the amount of underfocus. Images of the same virus particles with different underfocus values were combined to generate the original image reconstruction, which included information from

500 to 25 Å resolution (Stewart *et al.*, 1991). Rather than trying to match this combination, the reconstruction was recalculated with only the highest resolution images. We have used the equation given by Kenney *et al.* (1992) for the CTF with an additional Fermi filter to reduce high-resolution noise. The equation for the CTF with both phase and amplitude components is given by:

$$\text{CTF}(\nu) = \{(1 - F_{\text{amp}}) \times \sin[\chi(\nu)] + F_{\text{amp}} \times \cos[\chi(\nu)]\} \times e^{(-d\nu^2)}$$

where $\chi(\nu) = \pi\lambda\nu^2 (def - 0.5 \times Cs\lambda^2\nu^2)$, F_{amp} is the fraction of amplitude contrast, approximated as 0.10, ν is the spatial frequency in units of Å^{-1}, d is the decay factor in units of Å^2, def is the underfocus in μm, Cs is the spherical aberration of the microscope ($Cs = 1.6$ mm for the Phillips 400 microscope used in this work) and λ is the electron wavelength ($\lambda = 0.042$ Å for 80 kV electrons).

The equation for the Fermi filter is given by:

$$\text{Fermi}(\nu) = \frac{2}{1 + \exp[\ \min\{20, \max(0, (\nu - 1/\text{cutoff})/(2 \times tu))\}]}$$

where tu is the transform unit equal to 1/(dimension of the FFT $\times$ pixel size of the map in Å). The cutoff value was chosen as 25 Å, which is beyond the highest resolution of the data as estimated in the original reconstruction (Stewart *et al.*, 1991).

Two parameters, the underfocus value and the exponential decay factor, were found empirically by convolving a crystallographic hexon. To generate the crystallographic hexon density map the atomic numbers, or electron count, of the non-hydrogen atoms in a hexon trimer were summed within 7.3 Å^3 voxels, the size of the voxels in the reconstruction. This density map was convolved in reciprocal space. After an inverse three-dimensional Fourier transform, the reciprocal map values were multiplied by the Fermi filter and the CTF, which are both functions of spatial frequency. A three-dimensional Fourier transform then returned the map to real space. The parameter values that gave a hexon density map most similar to the hexons in the reconstruction were an underfocus of 2.5 μm and an exponential decay factor of 2000 Å^2. Two other sets of parameters that gave reasonable results were an underfocus of 2.0 μm with a decay factor of 3000 Å^2, and an underfocus of 1.5 μm with a decay factor of 3000 Å^2. Curiously, the best underfocus value for the deconvolution does not correspond to the actual defocus of the images, which is close to 1 μm. This emphasizes the fact that the CTF equation is only an approximation and that empirical tests with the crystallographic hexon were crucial.

Deconvolution of the image reconstruction was carried out in reciprocal space in an analogous manner to convolution of the hexon density. The reciprocal map values were multiplied by the Fermi filter value and divided by the CTF value (or a threshold of 0.02 to prevent division by zero).

Density fitting

A crystallographic hexon density map, calculated by summing the atomic numbers, was low-pass filtered to 25 Å resolution. Then the top 70 Å portion of the crystallographic hexon, which forms the distinct tower region, was cropped and used as the search model. Initial hexon positions were checked visually on a Stardent GS1000 graphics supercomputer using AVS software. Three translational and three rotational parameters were refined for each of the four hexon positions using a step search method by evaluating the cross-correlation coefficient for the search model with the deconvolved reconstruction. By positioning the crystallographic coordinates in the four refined sites and then applying 60-fold icosahedral symmetry, coordinates for a complete capsid of 240 hexons with >5 million non-hydrogen atoms were obtained. Transformation matrices to generate coordinates for a complete hexon capsid will be deposited in the Brookhaven Protein Data Bank along with the refined hexon coordinates (R.Murali and R.M.Burnett, in preparation). The rotations and translations to generate a capsid asymmetric unit from a hexon trimer are of course limited by the resolution of the EM reconstruction and are not as accurate as a complete crystallographic determination of the capsid would be. The atomic numbers were summed within 7.3 Å^3 voxels to generate a density map of the capsid, which was then low-pass filtered to 25 Å resolution. Including hydrogen atoms had no apparent effect on the hexon density.

Difference imaging

First the density in the disordered core (within a radius of 305 Å) of the deconvolved reconstruction was set to zero. Then the contrast was adjusted on the two maps to match the mean and standard deviation of the densities in the hexon portion of the deconvolved reconstruction, and in the filtered calculated capsid. In order to isolate the hexon portion of the reconstruction, a mask was created from the calculated capsid with every voxel above a cutoff density set to unity and every voxel below the cutoff set to zero.

Both the reconstruction and the calculated capsid were multiplied by the mask before calculating their mean and standard deviation values. Then a simple subtraction of the calculated capsid from the deconvolved reconstruction yielded a three-dimensional difference map. The scale of the EM map, which is determined to 2%, was not adjusted.

Several other approaches to difference imaging were tried, but did not work as well. These included: trying to find the parameters for the CTF equation by a least-squares fit of the radial density profiles from the calculated hexon capsid and the reconstruction (Kenney et al., 1992); not matching the mean and standard deviation of the two maps before subtraction; positioning the whole crystallographic hexon into the reconstruction rather than just the well-separated tower portion; positioning the crystallographic hexon tower density before deconvolution of the reconstruction; adding density maps for individual hexons rather than calculating the complete capsid density from its total atomic coordinates; generating a crystallographic hexon density map from calculated low-resolution structure factors. This last approach was fine for qualitative comparison of the crystallographic hexon with the reconstruction (Stewart et al., 1991), but truncation artifacts made it impractical for quantitative difference imaging.

Volume estimates

Individual density regions were cropped out of the difference map and volume estimates were obtained by summing the number of voxels above a specified contour level. This level was chosen as the point where the volume of the hexons in the deconvolved reconstruction changed the least with a fixed change in contour level. A volume/mass standard was obtained from hexon by dividing the total volume of the calculated hexon capsid by the mass of 240 trimers. The effect that the CTF parameters have on the measured volume was evaluated by deconvolving the image reconstruction using the two additional sets of parameters mentioned above, which gave reasonable results for one hexon. Difference imaging was repeated with careful scaling of the two maps and new contour levels were chosen. These two difference maps gave similar images of the penton base and volume measurements within 3% of the original value.

Updated stoichiometry

As the original stoichiometric analysis (van Oostrum and Burnett, 1985) relied on knowledge of the number of methionines in each mature polypeptide, this must be updated now that the cleavage sites of the adenovirus proteinase are better characterized (Anderson, 1990). The virally encoded proteinase cleaves three capsid polypeptides, IIIa, VI and VIII, from precursor molecules during virus maturation. For polypeptide IIIa, a cleavage site is found 15 residues from the C-terminus of the precursor. Assuming that the two N-terminal methionines are retained, the mature polypeptide would have 12 methionines to give an updated copy number of 68. The polypeptide VI precursor has two cleavage sites, removing 33 residues at the N-terminus and 11 residues at the C-terminus. The second cleavage site, which was not included in the van Oostrum and Burnett analysis, does not change the number of methionines or the copy number, but it does reduce the molecular mass of the mature component.

The polypeptide VIII precursor has three proteinase cleavage sites at its C-terminal end. If all sites are cleaved, the resulting polypeptide would have a smaller molecular mass than that observed, suggesting that only the middle or last two C-terminal sites are cleaved to yield a mature protein of 141 residues. The number of methionines in the mature polypeptide does not depend on which proteinase sites are cleaved, as all six methionines are found before the first potential cleavage site. However, the experimental copy number is affected by whether or not the N-terminal methionine is removed. Following van Oostrum and Burnett (1985), the presence of a serine residue at the second position favors removal to give five methionines and a copy number of 127 instead of 106. This value also seems more likely as it implies an integral copy number per icosahedral asymmetric unit.

The updated values shown in Table I have error ranges that reflect the precision of the five independent measurements made by van Oostrum and Burnett (1985). The true error range of the experiment, judged by the undisputed copy numbers of penton base and polypeptide IX, is at least four times the standard deviation. The copy numbers for all the polypeptides in the current model thus show excellent agreement with their experimental values except for polypeptide VI, which is off by just 1%.

Hexon gap density averaging

To reveal any non-artifactual difference density above the hexon towers, further averaging was performed. First, density from all of the assigned components was subtracted from the map. The remaining difference density was rotated and translated four times so that the molecular 3-fold axis of each hexon in the asymmetric unit was aligned along the z axis. These four maps were added then and then divided by a factor of four. To average around the 3-fold axis, this map was rotated by 120 and 240°. The original and two rotated maps were added, and then divided by a factor of three. The resulting averaged density was superimposed on top of a crystallographic hexon in the same orientation. The only strong density was found on top of the hexon towers. No density was found near the missing N-terminus of the crystallographic hexon.

Hexon gap modeling

In order to model the atoms of the 19 residue gap into the difference density above the hexon towers, positions for the C_α backbone were manually adjusted within semi-transparent difference density using AVS software on a Stardent GS1000 computer. A complete coordinate set for the 19 residue gap was generated using an extended backbone with a sharp turn in the middle and placing side chain atoms in their standard conformations. This structure was minimized (500 steps, Powell-method conjugate gradient) to remove the worst close contacts and to connect the stretch to the appropriate sites in the crystallographic hexon model. Then a short molecular dynamics simulation (600 steps, 1 fs time step, temperature 300°K and velocities rescaled every 25 steps) was carried out using X-PLOR version 3.0 (Brünger, 1992). Harmonic point restraints tethered the C_α atoms in the gap to the manually fitted points. Only the atoms in the 19 residue gap were allowed to move, while the rest of the hexon trimer was held fixed. A second short dynamics simulation was then run without using the point restraints and the resulting structure was minimized (500 steps, Powell-method conjugate gradient) to give the final model for the 19 gap residues.

Acknowledgements

References

Abad-Zapatero,C., Abdel-Meguid,S.S., Johnson,J.E., Leslie,A.G.W., Rayment,I., Rossmann,M.G., Suck,D. and Tsukihara,T. (1980) Nature, 286, 33–39.

Anderson,C.W. (1990) Virology, 177, 259–272.

Bancroft,J.B. (1970) Adv. Virus Res., 16, 99–134.

Boudin,M.-L., D'Halluin,J.-C., Cousin,C. and Boulanger,P. (1980) Virology, 101, 144–156.

Brown,D.T., Westphal,M., Burlingham,B.T., Winterhoff,U. and Doerfler,W. (1975) J. Virol., 16, 366–387.

Brünger,A.T. (1992) X-PLOR Version 3.0—A System for X-ray Crystallography and NMR Spectroscopy. Yale University Press, New Haven, CT.

Burnett,R.M., Grütter,M.G. and White,J.L. (1985) J. Mol. Biol., 185, 105–123.

Choi,H.-K., Tong,L., Minor,W., Dumas,P., Boege,U., Rossmann,M.G. and Wengler,G. (1991) Nature, 354, 37–43.

Colby,W.W. and Shenk,T. (1981) J. Virol., 39, 977–980.

Cuillel,M., Cortolezzis,B., Chroboczek,J., Langowski,J., Ruigrok,R.W.H. and Jacrot,B. (1990) Virology, 175, 222–231.

de Jong,J.C., Wigand,R., Kidd,A.H., Wadell,G., Kapsenberg,J.G., Muzeric,C.J., Wermenbol,A.G. and Firtzlaff,R.G. (1983) J. Med. Virol., 11, 215–231.

Everitt,E. and Philipson,L. (1974) Virology, 62, 253–269.

Everitt,E., Sundquist,B., Pettersson,U. and Philipson,L. (1973) Virology, 52, 130–147.

Everitt,E., Lutter,L. and Philipson,L. (1975) Virology, 67, 197–208.

Furcinitti,P.S., van Oostrum,J. and Burnett,R.M. (1989) EMBO J., 8, 3563–3570.

Green,N.M., Wrigley,N.G., Russell,W.C., Martin,S.R. and McLachlan,A.D. (1983) EMBO J., 2, 1357–1365.

Harrison,S.C., Olson,A.J., Schutt,C.E. and Winkler,F.K. (1978) Nature, 276, 368–373.

Kenney,J.M., Hantula,J., Fuller,S.D., Mindich,L., Ojala,P.M. and Bamford,D.H. (1992) Virology, 190, 635–644.

Newcomb,W.W., Boring,J.W. and Brown,J.C. (1984) J. Virol., 51, 52–56.

Roberts,M.M., White,J.L., Grütter,M.G. and Burnett,R.M. (1986) Science, 232, 1148–1151.

Robinson,I.K. and Harrison, S.C. (1982) Nature, 297, 563–568.

Rowe,W.P., Huebner,R.J., Gilmore,L.K., Parrott,R.H. and Ward,T.G. (1953) *Proc. Soc. Exp. Biol.*, **84**, 570−573.

Ruigrok,R.W.H., Barge,A., Albiges-Rizo,C. and Dayan,S. (1990) *J. Mol. Biol.*, **215**, 589−596.

Russell,W.C. and Precious,B. (1982) *J. Gen. Virol.*, **63**, 69−79.

Seth,P., Fitzgerald,D., Ginsberg,H., Willingham,M. and Pastan,I. (1984) *Mol. Cell. Biol.*, **4**, 1528−1533.

Stewart,P.L., Burnett,R.M., Cyrklaff,M. and Fuller,S.D. (1991) *Cell*, **67**, 145−154.

Stouten,P.F.W., Sander,C., Ruigrok,R.W.H. and Cusack,S. (1992) *J. Mol. Biol.*, **226**, 1073−1084.

Toogood,C.I.A., Murali,R., Burnett,R.M. and Hay,R.T. (1989) *J. Gen. Virol.*, **70**, 3203−3214.

Toogood,C.I.A., Crompton,J. and Hay,R.T. (1992) *J. Gen. Virol.*, **73**, 1429−1435.

van Oostrum,J. and Burnett,R.M. (1985) *J. Virol.*, **56**, 439−448.

van Oostrum,J., Smith,P.R., Mohraz,M. and Burnett,R.M. (1987) *Ann. NY Acad. Sci.*, **494**, 423−426.

Varga,M.J., Bergman,T. and Everitt,E. (1990) *J. Virol.*, **64**, 4217−4225.

Varga,M.J., Weibull,C. and Everitt,E. (1991) *J. Virol.*, **65**, 6061−6070.

Webster,A., Hay,R.T. and Kemp,G. (1993) *Cell*, **72**, 97−104.

Wohlfart, C. (1988) *J. Virol.*, **62**, 2321−2328.